

Long-Wavelength, Free-Free Spectral Energy Distributions from Porous Stellar Winds

R. Ignace^{*}

Department of Physics & Astronomy, East Tennessee State University, Johnson City, TN, 37614, USA

Accepted XXX. Received YYY; in original form ZZZ

ABSTRACT

The influence of macroclumps for free-free spectral energy distributions (SEDs) of ionized winds is considered. The goal is to emphasize distinctions between microclumping and macroclumping effects. Microclumping can alter SED slopes and flux levels if the volume filling factor of the clumps varies with radius; however, the modifications are independent of the clump geometry. To what extent does macroclumping alter SED slopes and flux levels? In addressing the question, two specific types of macroclump geometries are explored: shell fragments (“pancake”-shaped) and spherical clumps. Analytic and semi-analytic results are derived in the limiting case that clumps never obscure one another. Numerical calculations based on a porosity formalism is used when clumps do overlap. Under the assumptions of a constant expansion, isothermal, and fixed ionization wind, the fragment model leads to results that are essentially identical to the microclumping result. Mass-loss rate determinations are not affected by porosity effects for shell fragments. By contrast, spherical clumps can lead to a reduction in long-wavelength fluxes, but the reductions are only significant for extreme volume filling factors.

Key words: infrared: stars – radio: stars – stars: early-type – stars: mass-loss – stars: massive – stars: winds, outflows

1 INTRODUCTION

The issue of structured winds from massive stars stretches back several decades, and the prominence of wind “clumping” for influencing observables has steadily grown (e.g., Hamann et al. 2008). Evidence for clumping comes from a variety of indicators. The favored mechanism for explaining the winds of massive stars is the line-driven wind theory (Lucy & Solomon 1970; Castor et al. 1975; Pauldrach et al. 1986). Highly supersonic, massive star winds are driven outwards by the action of the UV-bright luminosities acting on metal line opacities. But the process is intrinsically unstable and naturally leads to structured flows (Lucy & Solomon 1970; Lucy & White 1980; Owocki et al. 1988; Macfarlane & Cassinelli 1989; Feldmeier et al. 1997; Dessart & Owocki 2003, 2005). Observationally, the evidence for structured massive-star winds is multi-wavelength in nature, including X-rays (e.g., Cassinelli & Swank 1983; Feldmeier et al. 2003; Nazé et al. 2013), the UV band, in the form discrete/narrow absorption components (e.g., Prinja & Howarth 1986; Massa et al. 1995; Prinja et al. 2012), and attempts to

explain certain UV-line strengths (e.g., Bouret et al. 2005; Fullerton et al. 2006; Oskinova et al. 2007; Zsargó et al. 2008; Sundqvist et al. 2010), optical recombination lines (Hillier 1991; Lépine & Moffat 1999), infrared excesses (e.g., Ignace 2009; Bonanos et al. 2009), longer wavelength emissions (e.g., Abbott et al. 1981; Puls et al. 2006; Blomme & Runacres 1997; Nugis et al. 1998; González & Cantó 2008), and polarimetry (e.g., Lupie & Nordsieck 1987; Taylor et al. 1991; Brown et al. 1995; Davies et al. 2007; Li et al. 2009).

The focus of this contribution is to expand the considerations of how “macroclumping” or “porosity” can influence observables of massive star winds in the infrared (IR) and radio regimes. In relation to the effect of clumping for inferring mass-loss rates, \dot{M} , many researchers invoke “microclumping”. Microclumping is the limit in which the radiative transfer is not impacted by the presence of clumping. For microclumping all clumps must be optically thin, and the radiative transfer calculations proceed essentially as if the flow is “smooth”. The influence of microclumping emerges in terms of the volume filling factor of clumps f_V , or an emissive enhancement factor (which is $1/f_V$, e.g. Hamann & Koesterke 1998; Ignace et al. 2003). The presence of clumping leads to an increase of the source flux relative to a smooth wind, and

* E-mail: ignace@etsu.edu

for microclumping the enhancement is unconnected to the specifics of the clump geometry, such as whether clumps take the form of spheres, filaments, flattened “pancake” structures, or any other shape.

By contrast, macroclumping deals with the case when the radiative transfer is influenced by the geometry of the clump structures (e.g., [Brown et al. 2004b](#)). For example, based on the expectations of the line-driving instability operating in massive star winds, [Oskinova et al. \(2004\)](#) invoked “shell fragments”, in the shape of flattened pancakes, to model a time-averaged spherical distribution of wind shocks to explain resolved X-ray emission profile shapes observed in massive stars. In a smooth wind, the line shapes should be significantly asymmetric (e.g., [Ignace 2001](#); [Owocki & Cohen 2001](#); [Ignace & Gayley 2002](#); [Leutenegger et al. 2007](#)). Clumping can alter the line profile shape for the emergent X-ray radiation. In particular, it can reduce line asymmetry (e.g., [Feldmeier et al. 2003](#); [Oskinova et al. 2004](#); [Owocki & Cohen 2006](#)).

In relation to the UV, initial results from a FUSE study of the PV doublet from massive star winds suggested dramatic reductions in mass-loss rates of O star winds owing to severe levels of clumping ([Fullerton et al. 2006](#)). The argument was that mass-loss rates from line profile fitting of UV lines is independent of wind clumping for an ion in its dominant stage. Comparing \dot{M} values from PV with those derived from clumping-dependent diagnostics (such as radio emissions) provides a measure of the volume filling factor for microclumping. However, the downward revisions were so severe as to change the expectations of stellar evolution models substantially ([Hirschi 2008](#)). One resolution¹ to the problem was found in a consideration of macroclumping ([Oskinova et al. 2007](#); [Šurlan et al. 2013](#)).

This paper extends consideration of macroclumping effects to the IR and radio bands. Others have also explored macroclumping for radio emissions, such as [Blomme & Runacres \(1997\)](#) and [González & Cantó \(2008\)](#). The former considered the impact of discrete shells and shell fragments on the long wavelength emission (but only for single shells or fragments). The latter considered an evolving shell, with application toward explaining variable radio emissions from P Cygni.

In this paper two particular clump geometries are contrasted: shell fragments and spherical clumps. Spherical clumps loosely represent the kinds of structures that can evolve from Rayleigh-Taylor instabilities. Rayleigh-Taylor instabilities lead to filamentary structures that can further devolve into “knots” and roundish clumps (e.g., [Ellinger et al. 2012](#)). For example, such effects can have relevance for the interaction of a wind and the interstellar medium (e.g., [Mohamed et al. 2012](#)). The shell fragments have long been a favorite for the highly supersonic massive star winds that are thought to be filled with shock structures (e.g., [Runacres & Owocki 2002](#)), although more recent simulations and observations now favor spherical clumps ([Dessart & Owocki 2003](#); [Leutenegger et al. 2013](#)). Discus-

¹ Macroclumping is not the only potential resolution. The presence of X-ray emissions could invalidate the assumption that PV is indeed the dominant ion stage for that element, as for example [Waldron & Cassinelli \(2010\)](#) and [Krtićka & Kubát \(2012\)](#).

sion of the problem begins with a review in § 2 of long-wavelength emissions from free-free opacity in a strictly smooth wind and in one with microclumping. An exploration of porosity effects for the IR/radio band in § 4 for the two different selected geometries. Concluding remarks are given in § 5.

2 SEDS FROM SMOOTH OR EFFECTIVELY SMOOTH WINDS

The objective of this work is to explore the consequences of macroclumping for IR/radio spectral energy distributions (SEDs) from ionized stellar winds. To do so, a number of simplifications are imposed to aid comparison of cases. For example, the model SEDs are restricted to free-free opacity. It is possible to include bound-free opacity as well, but at long wavelengths, its addition will have a similar scaling as the free-free opacity and will not impact qualitative and comparative trends described here. A focus on long wavelengths ensures that the wind will be optically thick, so thick that a pseudo-photosphere forms in the wind. In this case the continuum emission formed in the wind dominates the highly absorbed stellar emission at the wind base. Although massive star winds have overall declining temperature and varying ion fractions (e.g., [Drew 1989](#)), the wind at large radius tends to be more nearly isothermal with slowly varying ion fractions. For this study it is convenient to assume that the wind is isothermal with fixed ionization. Also, the flow is assumed to expand radially at constant speed (i.e., the wind terminal speed, v_∞).

Central to modeling the SEDs is the frequency-dependent optical depth, τ_ν . The optical depth from a distant observer to a point in the wind that lies along the line-of-sight (los) to the star center is given by

$$\tau_\nu = \int_{\tilde{r}}^{\infty} \kappa_\nu \rho R_* d\tilde{r}' \quad (1)$$

where κ_ν is the absorption coefficient and prime indicates a “dummy variable” for integration purposes. Tildes signify lengths that are normalized to the stellar radius, as for example $\tilde{l} = l/R_*$. The one exception will be the inverse radius, $u = R_*/r$, that will be used in a number of the integral expressions to be derived.

Working at relatively long wavelengths for hot-star winds, the Rayleigh-Jeans limit is adopted, for which $h\nu \ll kT$, and

$$\kappa_\nu \rho = 0.018 \frac{Z_i^2}{\mu_i \mu_e} \frac{\rho^2}{m_H^2} T^{-3/2} g_\nu \nu^{-2}, \quad (2)$$

where Z_i is the rms ion charge, μ_i and μ_e are mean molecular weights per free ion and per free electron, respectively, ρ is the mass density of the gas, m_H is the mass of hydrogen, T is the gas temperature, g_ν is the free-free Gaunt factor, and ν is the frequency of observation. The adopted assumptions imply that Z_i , μ_i , and μ_e are constants in the flow for this study.

The radial optical of equation (1) can be expressed as

$$\tau_\nu = \tau_0(\lambda) \int_{\tilde{r}}^{\infty} [\rho(\tilde{r}')/\rho_0]^2 d\tilde{r}', \quad (3)$$

where ρ_0 is the density at the base of the wind, and $\tau_0 = \kappa_0(\lambda) \rho_0 R_*$ is the characteristic optical depth scale as a function of wavelength, with $\kappa_0(\lambda) = \kappa(\lambda) \rho(\tilde{r})/\rho_0$. The latter is given by

$$\tau_0(\lambda) = 5 \times 10^5 \frac{Z_i^2}{\mu_i \mu_e} \rho_0^2 T_0^{-3/2} \left(\frac{R_*}{10R_\odot} \right) g_\nu \lambda_{\text{cm}}^2, \quad (4)$$

where fiducial density and temperature values of $\rho_0 = 10^{-13} \text{ g cm}^{-3}$ and $T_0 = 10^4 \text{ K}$ have been assumed, the stellar radius has been expressed in terms of ten solar radii, and the wavelength is given in centimeters. For a wind of completely ionized, pure hydrogen, ρ_0 would correspond to a number density of about 10^{11} cm^{-3} , which is characteristic of a wind with a mass-loss rate of $\dot{M} \sim 10^{-6} M_\odot \text{ yr}^{-1}$ and terminal speed 10^3 km s^{-1} , a fairly massive, evolved wind from an OB supergiant (e.g., [Muijres et al. 2012](#)). For such a wind, which is typical of the more extreme wind cases like WR stars, some OB supergiants, or LBV stars, the optical depth at 1 cm is enormous at the level of 10^6 .

2.1 Smooth Winds

Seminal works for the radio emissions from ionized, massive-star winds include [Wright & Barlow \(1975\)](#) and [Panagia & Felli \(1975\)](#). Both considered how to relate the radio emission to the wind mass-loss rate, assuming a smooth, spherical wind. The key results are that for an observer sightline through the spherical wind, the emergent intensity is

$$I_\nu = B_\nu(T) \left[1 - e^{-\tau_{\text{tot}}(\tilde{p})} \right], \quad (5)$$

where isothermality is assumed, τ_{tot} is the total optical depth of the wind along a ray of normalized impact parameter \tilde{p} , and B_ν is the Planck function. For a star of radius R_* at distance D from Earth, the emergent flux of radiation from the wind is then

$$F_\nu = 2\pi \frac{R_*^2}{D^2} B_\nu(T) \int_0^\infty \left[1 - e^{-\tau_{\text{tot}}(\tilde{p})} \right] \tilde{p} d\tilde{p}. \quad (6)$$

At long wavelengths where the wind density is an inverse square law, and the wind emission can be considered to dwarf the stellar emission (which is also highly absorbed), the optical depth factor takes on the form $\tau_{\text{tot}} = K(\lambda) \tilde{p}^{-3}$, where the stellar, wind, and wavelength parameters of the opacity are collected in the wavelength-dependent factor K . In this case the integral can be analytically evaluated.

[Cassinelli & Hartmann \(1977\)](#) described how free-free flux that forms in the wind could be interpreted in terms of a pseudo-photosphere. Their argument was to evaluate an effective photospheric radius r_{eff} where $\tau_\nu = 1/3$ along the los. From equation (3), one obtains

$$r_{\text{eff}} = [3 \tau_0(\lambda)]^{1/3} R_* \propto g_\nu^{1/3} \lambda^{2/3} R_*. \quad (7)$$

Using fiducials of $\rho_0 = 10^{-13} \text{ g cm}^{-3}$, $T_0 = 10^4 \text{ K}$, and assuming $g_\nu = 1$, the effective radius of the pseudo-photosphere will be $r_{\text{eff}} \approx 80R_*$ at a wavelength of 1 cm.

The flux then becomes

$$F_\nu = \frac{L_\nu}{4\pi D^2} = \frac{1}{4} B_\nu(T) r_{\text{eff}}^2 \propto g_\nu^{2/3} \lambda^{-2/3}. \quad (8)$$

With $g_\nu \propto \lambda^{0.11}$ in the radio band ([Cox 2000](#)), the radio SED is a power law with a logarithmic slope exponent of about -0.6 with λ . Observations of this value generally signal that the wind is isothermal, spherical, and at terminal speed. Slight deviations, especially somewhat steeper negative slopes, may indicate variations in the temperature or ionization of the wind. For the Rayleigh-Jeans limit, [Cassinelli & Hartmann \(1977\)](#) generalized their results to relate an observed SED slope in terms of power-law exponents for the density and temperature distributions.

Alternatively, deviations from the standard value of -0.6 may also indicate that the free-free emission forms in the wind acceleration zone, which is relevant to lower density winds. A rising velocity steepens the density with consequence for the observed SED. A positive slope would be non-thermal, generally interpreted as related to synchrotron emission and the presence of magnetism in the extended wind (e.g., [Blomme 2011](#)).

In this paper the wind is assumed isothermal, with an ionization structure that is constant throughout, and for simplicity the spherical wind will be taken to expand at constant speed. In this situation the formal solution for the optical depth along any sightline traversing the spherical wind is given by

$$\tau(z, \tilde{p}) = \frac{\tau_0(\lambda)}{2\tilde{p}^3} [\theta - \sin(\theta) \cos(\theta)], \quad (9)$$

where $\tilde{z} = \tilde{p}/\tan(\theta)$.

In the limit of large optical depth with $\tau_0 \gg 1$, the “pseudo-photosphere” formed by the wind completely absorbs the direct emission by the stellar photosphere, and the continuum emission is considered “wind-dominated”. At wavelengths where $\tau_0 \ll 1$, the wind emission is small, the absorption of direct starlight is negligible, and the continuum is said to be “star-dominated”. Although model SEDs will properly account for the starlight component, the discussion of fluxes will generally focus on the wind contribution and ignore the the stellar contribution.

The integration for flux requires the total optical depth, τ_{tot} for a los of fixed impact parameter \tilde{p} . Its value is given by equation (9) for $\theta = \pi/2$, with $\tau_{\text{tot}} = \pi \tau_0/2\tilde{p}^3$. Ignoring the stellar contribution as justified above, the solution for the flux of emission by the wind is

$$F_\nu \approx 2\pi \frac{R_*^2}{D^2} B_\nu(T_w) \int_0^\infty \left(1 - e^{-\pi \tau_0/2\tilde{p}^3} \right) \tilde{p} d\tilde{p}, \quad (10)$$

Appendix A) details the steps to obtaining an analytic solution for this integral, with the result,

$$F_{\text{sm}} = F_\nu = \frac{2}{3} \Gamma \left(\frac{1}{3} \right) \times \frac{\pi R_*^2}{D^2} B_\nu(T_w) \left[\frac{\pi \tau_0(\lambda)}{2} \right]^{2/3}, \quad (11)$$

where the subscript “sm” signifies the smooth wind result, and Γ is the “Gamma” function. [Wright & Barlow \(1975\)](#) showed that this expression corresponds to a pseudo-photosphere of effective radius where the line-of-sight optical depth achieves $\tau(\lambda) = 2\pi^2/81 = 0.244$. [Hillier et al.](#)

(1983) considered a different measure. They estimated the optical depth at which a volume integral of the emissivity would achieve the required flux. This “effective volume” corresponds to an integration of the free-free emissivity beyond $\tau(\lambda) = (2/3\pi) (3/8)^{3/2} = 0.049$.

2.2 Winds with Microclumping

A feature of the radio-band emission is the opportunity to infer the mass-loss rate of the wind. The scale of the flux is set by $(\dot{M}/v_\infty)^{2/3}$. Since the wind terminal speed can be independently constrained from wind-broadened lines (e.g., [Prinja et al. 1991](#)), observed radio fluxes can be used to infer wind \dot{M} values, which has been pursued by numerous researchers (e.g., [Abbott et al. 1986](#); [Biegging et al. 1989](#); [Leitherer et al. 1995](#)). However, evidence for the influence of clumping effects became apparent through a variety of diagnostics, as described in § 1. The question arises of how clumping impacts the long-wavelength emissions.

Many have adopted a model of “microclumping” to infer better \dot{M} values from radio studies of dense winds. Microclumping is the limit in which all individual clump structures are optically thin. The radiative transport through such a flow is the same as for a smooth wind, but with a correction factor. Thus microclumping is “effectively smooth” in its treatment of the flux calculation. Microclumping does not alter the SED slope as compared to a smooth wind approach (e.g., [Nugis et al. 1998](#)), but it does alter inferred values of \dot{M} .

Because the free-free opacity scales as ρ^2 , clumping generates more optically thin emission per unit volume as compared to an unclumped wind. Defining f_V as the volume filling factor for the clumping, mass-loss rates are lowered by the multiplicative factor, $\sqrt{f_V}$ (i.e., for f_V constant throughout the wind), as compared to no clumping. This is derived next, and will be used as a reference against which to compare macroclumping results.

Let $\langle \rho \rangle$ be the volume-averaged wind density. Let ρ_{sm} be the unclumped, smooth wind density for a spherical wind with

$$\rho_{\text{sm}} = \frac{\dot{M}}{4\pi r^2 v(r)}, \quad (12)$$

where $v(r)$ is the velocity law of the wind. The density of clumps with microclumping becomes

$$\rho_{\text{mic}} = \frac{1}{f_V} \times \frac{\dot{M}}{4\pi r^2 v(r)}. \quad (13)$$

The form of the wind speed will be irrelevant, as the focus of applications is on asymptotic results for thick winds where the observed free-free emission forms at large radii. At large radius, $v(r) \approx v_\infty$.

When calculating the optical depth integral, the factor $\kappa_{\nu\rho} \propto \rho_{\text{mic}}^2 \propto f_V^{-2}$. However, the clumps are encountered only over a fraction of the integration path length, namely the fraction f_V . Consequently, for microclumping, the optical depth becomes

$$\tau_{\text{mic}} = \tau_{\text{sm}}/f_V, \quad (14)$$

where τ_{sm} is the optical depth for a smooth wind of the same \dot{M} , R_* , and wind velocity profile. The expression for the flux of emission, when the wind is optically thick follows from equation (11):

$$F_{\text{mic}} = \frac{1}{f_V^{2/3}} \times F_{\text{sm}} \quad (15)$$

which is the well-known result that for a given mass-loss rate, microclumping enhances the flux of emission by a factor $f_V^{-2/3}$. To ignore wind clumping would imply overestimating the wind mass-loss rate by a factor $f_V^{-1/2}$, since $F_{\text{sm}} \propto \dot{M}^{4/3}$ and $F_{\text{mic}} \propto (\dot{M}^2/f_V)^{2/3}$.

However, there is the possibility that the clumps are not optically thin, in which case the radiative transport must take account of the clump geometry (e.g., [Brown et al. 2004a](#)), a situation that has been dubbed macroclumping (e.g., [Oskinova et al. 2007](#)). The opacity at long wavelengths scales as λ^2 . Clump structures that are optically thin at shorter wavelengths can become optically thick at longer ones, thus the degree to which stochastically structured flows may be treated as microclumping versus macroclumping is a λ -dependent consideration.

3 WINDS WITH MACROCLUMPING: SPECIAL CASE WITH DISCRETE CLUMPS

The radiative transfer through macroclumps requires specification of the clumps themselves, as for example the investigations of [Feldmeier et al. \(2003\)](#) and [Oskinova et al. \(2004\)](#). Ultimately a realization of the structured flow must be imposed, and then the radiative transport can be numerically evaluated by shooting rays through the medium to compute emergent intensities and then fluxes for unresolved sources. [Oskinova et al. \(2004\)](#) use a discrete approach for the simulation of X-ray observables.

An alternative approach has been described under the heading of porosity. [Owocki & Cohen \(2006\)](#) simulate the effects of macroclumping with integral relations based on probabilistic considerations associated with the radiative transfer. The approach relies on constructing an effective opacity for expressing the consequences of macroclumping (e.g., [Sundqvist et al. 2012, 2014](#)). The porosity formalism is adopted in the radiative transport for calculations of the free-free fluxes from winds.

However, before pursuing a solution for the full radiation transport through the clumped outflow, there is a special circumstance that can be instructive to consider. Imagine that clumped structures are sparsely distributed such that from the observer point-of-view, no clumps overlap each other as projected on the sky. Further suppose that the solution for a given clump is $\delta F_{\nu,i}$. Then the flux for the ensemble total becomes

$$F_\nu = \sum_i^N \delta F_{\nu,i}. \quad (16)$$

In the limit that clumps are numerous, the sum can be represented in integral form:

$$F_\nu = \int n_{\text{cl}}(\tilde{r}, \mu, \phi) R_*^3 \delta F_\nu(\tilde{r}, \mu, \phi) \tilde{r}^2 d\tilde{r} d\mu d\phi, \quad (17)$$

where $\mu = \cos(\theta)$ and n_{cl} is the number density of clumps distributed throughout the wind.

The models under consideration will be for large optical depths for asymptotic conditions with the emission forming at large radius where the wind is at terminal speed v_∞ . For a uniform distribution, the number density of clumps is

$$n_{\text{cl}} = \frac{\dot{N}_0}{4\pi r^2 v_\infty}, \quad (18)$$

where \dot{N}_0 is the injection rate of clumps into the flow at the wind base.

Note that the complete absence of overlap among the ensemble is actually too strong a requirement. What matters is that the cumulative optical depth arising from any overlap be optically thin. This was the limit implicitly used in the application by Ignace & Churchwell (2004, hereafter ‘‘IC’’) to explain radio SEDs from ultracompact HII regions. This special case will be referred to as the ‘‘sparse’’ limit, even though the overlap of structures that are optically thin is formally allowed.

In order to employ the sparse limit expressions, the nature of the macroclumps must be specified. Here two cases are considered: shell fragments and spherical clumps. Both will be taken as having constant density within their boundaries, but with densities that depend on location in the wind flow. A spherical clump offers the same flux no matter from what direction it is viewed, but the intensity distribution across the clump is not uniform (i.e., spherical clumps are brighter along their diameter than at their limb). By contrast the shell fragments will be treated as circular ‘‘pancake’’ shapes. The projected shape of a shell fragment when viewed obliquely is elliptical. In contrast to spherical clumps, the intensity across a shell fragment is uniform (i.e., ignoring edge effects given that the fragments are assumed to be geometrically thin). Evidently different clump structures offer different source properties, and these can impact their ensemble trends.

3.1 Sparse Flattened Shell Fragments

Shell fragment clumps, with outward normals directed along radials from the star, may represent compressed structures from shocked gas. One-dimensional, time-dependent, hydrodynamic simulations predict highly structured winds in terms of dense shells separated by zones of highly rarified gas.

However, the 1D models overpredict the variability of X-rays from massive stars. Although results for ζ Pup clearly indicate X-ray variability, the number of discretized, non-spherical clumps implied seems large (Nazé et al. 2013). Two-dimensional simulations by Dessart & Owocki (2003, 2005) suggest that a highly structured flow can form. Although 3D models have not been presented, 1D and 2D simulations have led to a picture of a wind flow in which the majority of the matter exists in a fairly random distribution of clumps.

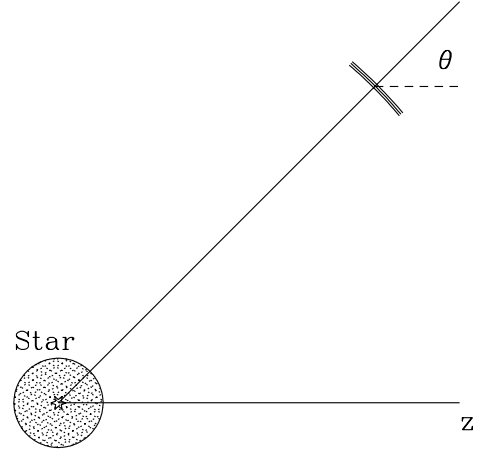


Figure 1. Geometry for the shell fragment clump. In cross-section a shell fragment is a thin line that is normal to a radial from the star. Here the observer is along the z -axis and views the shell fragment at an oblique angle θ .

Feldmeier et al. (2003) described the radiative transport of X-ray emissions through shell fragments. Although at IR and radio wavelengths, the opacity is different (ρ^2 for free-free opacity versus ρ for photoabsorptive opacity of X-rays), the geometrical considerations are similar. One important difference is that for the X-ray problem, the pancake structures consist of a hot plasma component adjacent to a cool one. It is the cool one that does the photoabsorbing; the hot plasma produces optically thin emission. For the free-free situation, the emission and absorption both occur in the same material, in this case the cooler component².

Following Feldmeier *et al.*, the optical depth through a shell fragment along a ray that intersects it at an oblique angle θ from the normal will be given by

$$\tau_z = \frac{\tau_r}{|\mu|}, \quad (19)$$

where $\mu = \cos \theta$, z signifies the observer axis (see Fig. 1), and τ_r is the optical depth normal to the shell fragment. Note that this optical depth is taken as a constant across the fragment.

For the optical depth along a radial that passes through a shell fragment, it is tempting to assume that the density is inverse square by assuming that the fragment evolve through the flow at constant solid angle, $\delta\Omega$. However, this is not obvious. The fact that the fragment represents a shock implies

² Since the free-free opacity drops as $T^{-3/2}$, and the X-ray emitting plasma is two orders of magnitude hotter than the cooler gas, any hot component existing at large radius as an ‘‘inter-clump’’ component will be optically thin compared to the cool clump component. Also, the optically thin free-free emissivity scales as density squared. The hot component can reasonably be ignored as a contributor to the long-wavelength free-free emission.

that matter may accumulate in it, which would make the density less steep than inverse square (e.g., Gayley 2012). On the other hand, the lateral width of the fragment can expand owing to gas pressure, resulting in an evolving solid angle for the fragment.

For simplicity the density within a fragment is taken to decline with the radius of its center as a power law, with \tilde{r}^{-q} . The optical depth is

$$\tau_z = \tau_0(\lambda) \mu^{-1} \delta\tilde{r}^{-2q}, \quad (20)$$

where

$$\tau_0 = \kappa_0 \rho_0 R_* \delta\tilde{r}_0, \quad (21)$$

with δr_0 the radial width of a fragment at the base of the wind.

The intensity along a ray that is oblique through a fragment is given by:

$$I_\nu = 2\pi B_\nu \left[1 - e^{-\tau_0 \mu^{-1} \tilde{r}^{-2q}} \right]. \quad (22)$$

Again, this assumes that the radial optical depth τ_r is constant across the face of the shell fragment. The flux is $\delta F_\nu = \delta\Omega \mu I_\nu (r^2/D^2)$.

Given a time-averaged spherically symmetric and sparse distribution of clumps, and using equation (17), the solution for the total flux from an ensemble of such structures, all of the same solid angle extent, becomes

$$F_\nu = B_\nu \delta\Omega \frac{R_*^2}{D^2} \frac{\dot{N}_0}{v_\infty/R_*} \int_0^1 \int_1^\infty \left[1 - e^{-\tau_0 \mu^{-1} \tilde{r}^{-2q}} \right] \tilde{r}^2 d\tilde{r}. \quad (23)$$

The ratio v_∞/R_* is a flow rate of clumps over the scale of the stellar radius, which is the scale of the wind density, whereas \dot{N}_0 is the injection rate of clumps into the flow. Hence the ratio $\dot{N}_0/(v_\infty/R_*)$ represents a relative clustering of clumps along a radial.

In equation (23), the integration over μ reflects the fact that the circular shell fragments, when seen oblique to the normal, appear as ellipses of uniform brightness I_ν (for a given fragment) and area $\mu \delta\Omega R_*^2$. Note that the optical depth appears to diverge as $\mu \rightarrow 0$, which is unphysical; however, in this model such edge-on fragments also have zero area and so never contribute to the flux.

The solution for the flux would be analytic if the lower limit for the integration in radius were to extend to zero. As in previous works (c.f., Wright & Barlow 1975), changing the lower limit from 1 to 0 is acceptable for long wavelengths where $\tau_0 \gg 1$. A general solution to integrals with the form of equation (23) is

$$\int_0^\infty \left[1 - e^{-ax^{-b}} \right] r^2 dr = a^{3/b} \left[\frac{-\Gamma(-3/b)}{b} \right], \quad (24)$$

if $b > 3$. For the application of interest, the solution is

$$F_\nu = \pi B_\nu \frac{\delta\Omega R_*^2}{D^2} \frac{\dot{N}_0}{v_\infty/R_*} \int_0^1 \left(\frac{\tau_0}{\mu} \right)^{3/2q} \left[\frac{-\Gamma(-3/2q)}{2q} \right] \mu d\mu. \quad (25)$$

Evaluating the integral in μ and manipulating the integration constants yields

$$F_\nu = \frac{2q/3}{4q-3} \Gamma\left(1 - \frac{3}{2q}\right) \tau_0^{3/2q} \times \pi B_\nu \frac{\delta\Omega R_*^2}{D^2} \frac{\dot{N}_0}{v_\infty/R_*}. \quad (26)$$

Note that with $q = 2$ for an inverse square law density, the SED would be $F_\nu \propto g_\nu^{0.75} \lambda^{-0.5} \sim \lambda^{-0.42}$. This is a fairly shallow SED slope. The well-known SED slope of -0.6 for a smooth wind occurs when $q \approx 5/4$.

3.2 Sparse Spherical Clumps

The results presented here for spherical clumps are an extension of the method discussed in IC, who considered an application of the free-free emission from constant density, spherical clumps to explain anomalous SED slopes seen in some ultra-compact H II regions. Here the approach of IC is applied to a time-averaged spherical wind. Unlike the interstellar situation, application to a stellar wind imposes a characteristic optical depth distribution for an ensemble of clumps owing to the nature of the clumps partaking in a spherical outflow. Consider the SED from a single isolated clump. IC showed (also in Osterbrock 1989) that the flux of emission from a single clump is given by

$$F_\nu = \frac{R_*^2}{D^2} \pi B_\nu G(\tau_{cl}), \quad (27)$$

where τ_{cl} is the optical depth along the diameter of the spherical clump which $\kappa_\nu \rho$ constant within its interior, as given by

$$\tau_{cl} = 2 \kappa_\nu(\rho_{cl}, \lambda) \rho_{cl} R_{cl}, \quad (28)$$

Note that equation (27) is based on equation (4) from IC, but corrects for an errant factor of 2 that should not have been present in IC.

The function $G(\tau_{cl})$ is given by

$$G(\tau_{cl}) = 1 - \frac{2}{\tau_{cl}^2} \left[1 - (1 + \tau_{cl}) e^{-\tau_{cl}} \right]. \quad (29)$$

At large optical depth with $\tau_{cl} \gg 1$, $G \approx 1$. At the opposite extreme of $\tau_{cl} \ll 1$, $G \approx 2\tau_{cl}/3$, which is the area-averaged value across the sphere.

The optical depth τ_{cl} along the diameter of a clump located at radius \tilde{r} can be expressed as

$$\tau_{cl}(\tilde{r}) = \tau_0(\lambda) \left(\frac{\rho_{cl}^2 R_{cl}}{\rho_0^2 R_0} \right), \quad (30)$$

where ρ_0 and R_0 are fiducial values. The density within the clump is constant, but the question of how that density varies with radius in the wind must be addressed. One might consider spherical clumps to maintain constant solid angle, like the fragment clump case. In order to maintain spherical shape, this would imply that $R_{cl} \propto r$, and so $\rho_{cl} \propto r^{-3}$. However, the reference case involves a density that drops as r^{-2} . Imposing $\rho_{cl} \propto r^{-2}$ means that spherical clumps do not expand at constant solid angle.

To allow for greater generality, the form $\rho_{cl} \propto \tilde{r}^{-m}$ is adopted. Mass conservation for a clump requires that

$R_{\text{cl}}^3 \rho_{\text{cl}} = \text{constant}$, and so $R_{\text{cl}} \propto \tilde{r}^{m/3}$. As a result, the position-dependent optical depth of a spherical clump becomes

$$\tau_{\text{cl}} = \tau_0(\lambda) \tilde{r}^{5m/3}. \quad (31)$$

Note that spherical clumps have been used in considerations by Oskinova et al. (2007) and Ignace et al. (2012). It is not uncommon for a spherical shell to “fragment” into elongated features ala a Rayleigh-Taylor instability, and these in turn can further break up into ball-shaped structures. Dessart & Owocki (2005) observe this effect in their 2D simulations for time-dependent line-driven winds. Their models show that wind structures develop rings that are round in cross-section, rather than flat, lending support to the idea that roughly spherical clumps could form. Consequently, at any given time, a snapshot of the flow would possess a component comprised of spherical clumps.

For the case of sparse clumps, the total emergent flux from the ensemble is:

$$F_\nu = \pi B_\nu \frac{R_{\text{cl}}^2}{D^2} \int_1^\infty n_{\text{cl}}(\tilde{r}') G(\tau_{\text{cl}}) 4\pi \tilde{r}'^2 d\tilde{r}' \quad (32)$$

$$= \pi B_\nu \frac{R_{\text{cl}}^2}{D^2} \frac{\dot{N}_0}{v_\infty/R_*} \int_1^\infty G[\tau_{\text{cl}}(\tilde{r}')] d\tilde{r}'. \quad (33)$$

At this point it is useful to adopt a change of variable from normalized radius x to optical depth τ_{cl} for the integration. Let the largest value of τ_{cl} be τ_{max} for a clump located at $x = 1$. Then $x = (\tau_{\text{cl}}/\tau_{\text{max}})^{-3/5m}$. The integration that was over the clump ensemble in spatial location becomes one over the clump ensemble in optical depth space (similar in spirit to the work of IC), with

$$F_\nu = \frac{3}{5m} F_0(\lambda) \tau_{\text{max}}^{\gamma-1} \int_0^{\tau_{\text{max}}} \tau_{\text{cl}}^{-\gamma} G(\tau_{\text{cl}}) d\tau_{\text{cl}}, \quad (34)$$

where

$$\gamma = \frac{3+7m}{5m}, \quad (35)$$

and

$$F_0 = \pi B_\nu \frac{R_{\text{cl}}^2}{D^2}. \quad (36)$$

One of the interesting attributes of equation (34) is the wavelength dependence of the factors appearing in front of the integral. In the Rayleigh-Jeans limit, the product of the Planck function and τ_{max} yields a power law with

$$B_\nu \tau_{\text{max}}^{\gamma-1} \propto g_\nu^{\gamma-1} \lambda^{-4+2\gamma}. \quad (37)$$

The integral itself contributes an additional wavelength dependence via the upper limit τ_{max} . Given that $m = 2$ and $m = 3$ are the relevant density power-laws of interest, γ equals 1.7 and 1.6, respectively. The factors outside the integral, using $g_\nu \propto \lambda^{0.11}$, give corresponding wavelength dependences of $\lambda^{-0.53}$ for $m = 2$ and $\lambda^{-0.72}$ for $m = 3$. At long wavelengths such that $\tau_{\text{max}} \gg 1$, the integral factor has only a weak dependence on λ . The reason is that the factor $\tau_{\text{cl}}^{-\gamma}$ in the integrand dominates such that most of the integration

is set at low and modest values of τ_{cl} . At long wavelengths the integral is well-approximated as a constant (but one that depends on m), and the SED slope is determined primarily by the factors outside the integral, which for $m = 2$ and 3 bracket the canonical result of -0.6 for microclumping.

Note that these results assume a universal size for clumps at the inner wind radius. It is straightforward to introduce a distribution of clump sizes. Suppose that \mathcal{P}_{cl} is the probability for a clump to have a radius R_{cl} in the interval of R_{min} to R_{max} . Then the flux for an ensemble of sizes would proceed as follows.

The result of equation (34) is now indicated by \hat{F}_ν for the SED contribution from clumps that have a size R_{cl} . For a range of sizes, the flux becomes

$$F_\nu = \int_{R_{\text{min}}}^{R_{\text{max}}} \mathcal{P}(R_{\text{cl}}) \hat{F}_\nu(R_{\text{cl}}) dR_{\text{cl}}, \quad (38)$$

where the probability distribution is normalized, with

$$\int_{R_{\text{min}}}^{R_{\text{max}}} \mathcal{P}(R_{\text{cl}}) dR_{\text{cl}} = 1. \quad (39)$$

The influence of a range of sizes affects the SED calculation in two ways. First, there is an overall factor of R_{cl}^2 in F_0 , so smaller clumps tend to be less bright. Second, assuming that all clumps have the same initial density, smaller clumps tend to be more optically thin, which makes them less bright, and further means that they become optically thick at longer wavelengths as compared to bigger clumps.

Figure 2 shows SEDs for a clump distribution, $\mathcal{P}_{\text{cl}} \propto R_{\text{cl}}^{-\beta}$, with values of $\beta = 0, 1, 2$, and 3, from top to bottom. The examples are designed to display the relative effect from having a greater representation of small clumps. The magenta indicates the asymptotic SED value. These models are for $m = 2$. An ensemble of clump sizes does not change the SED asymptote, only the brightness level and where in wavelength the wind emission begins to dominate the stellar component.

4 WINDS WITH MACROCLUMPING: POROSITY APPROACH

The preceding discussion of the sparse limit shows that the geometry of the clumps can affect both the SED slope and the flux level. However, one generally expects that multiple clumps will lie along a given sightline. In such cases of overlap, the radiative transfer is more complicated. The emission by each rearward clump along a los must be attenuated by all the clumps intervening between it and the observer, with corresponding emission increments for each.

Several researchers have considered the radiative transfer in porous, massive star winds both for diagnostics such as X-ray and UV lines (Feldmeier et al. 2003; Oskinova et al. 2004; Owocki & Cohen 2006; Oskinova et al. 2007; Sundqvist et al. 2012, 2014), and in terms of wind-driving physics such as super-Eddington and line-driven flows (Owocki et al. 2004; Sundqvist et al. 2014). Here the use of the porosity formalism is brought to bear on the problem of continuum free-free emission.

The porosity approach is a way of expressing discrete

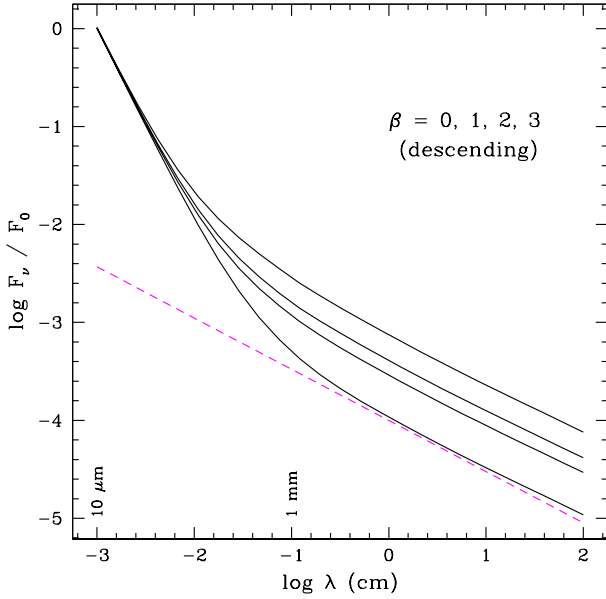


Figure 2. SEDs for spherical clumps in the sparse limit with a distribution in clump sizes R_{cl} . In these four models, β signifies power-law distributions for clump sizes. The case of $\beta = 0$ is a flat distribution (clumps of different sizes are all equally likely, within a specified range); increasing β results in increasingly more small clumps as compared to large ones. All the models have the same number of clumps and same optical depth parameter.

sums over clump structures for the radiative transfer along a sightline in terms of integral expressions. The result reduces to the microclumping case when clumps are optically thin. It is when individual clumps become optically thick that the clump geometry must be considered. The ability to move from discrete sums to integral expressions is the opposite of the sparse limit: for the sparse limit, the radiative transfer is confined to individual clumps; porosity allows for multiple clumps along a sightline.

Feldmeier et al. (2003) showed that the effective optical depth along a sightline through a porous wind is given by

$$\tau = \int \left[\int n_{\text{cl}} R_*^3 (1 - e^{-\tau_{\text{cl}}}) d\tilde{A}_{\text{cl}} \right] d\tilde{z}, \quad (40)$$

where \tilde{A}_{cl} is the normalized projected area of the clump toward the observer. The inner integration is across the face of the clump; the outer is through the wind. The interpretation is that the product $n_{\text{cl}} R_*^3 d\tilde{A}_{\text{cl}} d\tilde{z}$ is the number of clumps encountered in a differential unit of volume. The factor $(1 - \exp(-\tau_{\text{cl}}))$ is the fraction of light absorbed by a clump at this location, with τ_{cl} the optical depth of the clump along the ray. Clearly, if $\tau_{\text{cl}} \ll 1$, the effective optical depth is just the cumulative optical depth for the los in the interval $d\tilde{z}$. However, when $\tau_{\text{cl}} \gg 1$, the effective optical depth by clumps.

Regarding this last point, the normalized porosity length is defined as $\tilde{h} = h/R_* = (n_{\text{cl}} A_{\text{cl}} R_*)^{-1}$ and repre-

sents the mean free path between clumps along a sightline. For thick clumps, the effective optical depth becomes

$$\tau = \int d\tilde{z}/\tilde{h}. \quad (41)$$

This amounts to the number of mean free paths along the los. Consequently, even if clumps are quite optically thick, it may be that τ can be relatively small if the environment is highly porous (i.e., $\tilde{h} \gg 1$).

4.1 Porosity with Fragments

Consider again the pancake-shaped shell fragment in projection. For a geometrically thin clump of not overly large solid angle, such a fragment appears elliptical in shape and is uniformly bright across its projected face. The porosity length for a distribution of fragments is

$$\tilde{h} = \frac{1}{n_{\text{cl}} \mu A_{\text{cl}} R_*} = \left(\frac{v_{\infty}/R_*}{\dot{N}_0} \right) \left(\frac{4\pi}{\mu \delta\Omega} \right). \quad (42)$$

The shell fragments have a porosity length that depends on μ , or location around the star. For the outer wind that is at terminal speed, \tilde{h} does not vary with distance from the star, but does vary with location about the star. The associated volume filling factor for shell fragments is

$$f_V = n_c V_c = n_c A_c R_* \delta\tilde{l}_0 = \frac{\dot{N}_0}{v_{\infty}/R_*} \left(\frac{\mu \delta\Omega}{4\pi} \right) \delta\tilde{l}_0, \quad (43)$$

where V_c is a volume over which the filling factor is determined, and $\delta\tilde{l}_0$ is the normalized radial width of the fragment. This width could be a function of radius, but will be taken as constant in the discussion that follows.

The expression for the optical depth to position $u = 1/x$ along the los to the star center (i.e., $\mu = 1$) is given by

$$\tau = \frac{\tau_0}{f_0} \int_0^u \left[\frac{1 - e^{-\tau_{\text{cl}}}}{\tau_{\text{cl}}} \right] u^2 du, \quad (44)$$

where $f_V = f_0 \mu$,

$$f_0 = \frac{\dot{N}_0}{v_{\infty}/R_*} \left(\frac{\delta\Omega}{4\pi} \right) \delta\tilde{l}_0, \quad (45)$$

and

$$\tau_{\text{cl}} = \left(\frac{\tau_0}{f_0} \right) \left(\frac{\delta\tilde{l}_0}{f_0} \right) \left(\frac{u^4}{\mu} \right). \quad (46)$$

The bracketed factor in equation (44) is the form of an escape probability. At low values of τ_{cl} , the factor reduces to unity, in which case the microclumping limit is recovered. For large τ_{cl} , the factor reduces to $1/\tau_{\text{cl}}$, so that the effective optical depth when clumps become thick can be much suppressed with macroclumping as compared to microclumping.

The left side of Figure 3 shows the optical depth for a sightline along a radial to the star based on equation (44). The figure compares the porosity case against the microclumping assumption, ignoring the fact that the clumps are optically thick. The volume filling factors are $f_0 = 0.01$ (magenta), 0.04, 0.09, 0.16, and 0.25 (black), all with $\tau_0 = 300$.

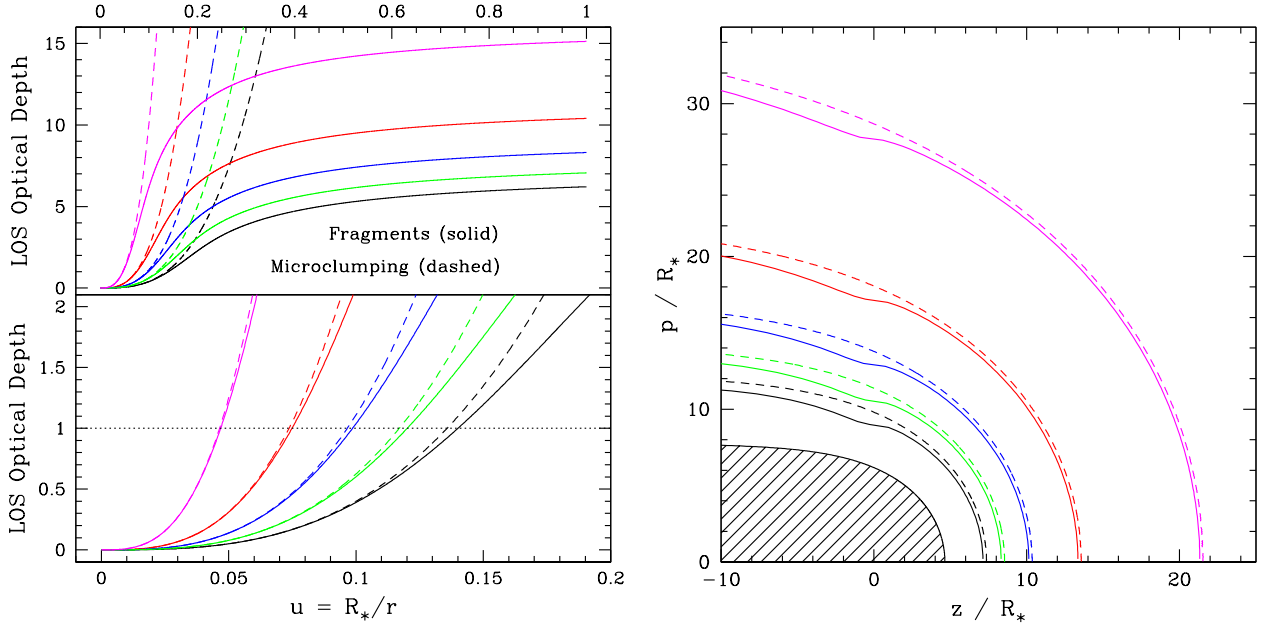


Figure 3. Left: The line-of-sight (los) optical depth as a function of normalized inverse radius u as compared with microclumping for a range of volume filling factors. Upper panel is for the full range of u from 0 to 1; lower is for small u (i.e., $r \gg R_*$) to highlight the region where microclumping and porosity diverge. The volume filling factors are for $f_0 = 0.01$ (magenta), 0.04, 0.09, 0.16, and 0.25 (black). Right: Associated contours for optical depth unity in the $z - p$ plane. The color scheme and line types are the same as in the left panel.

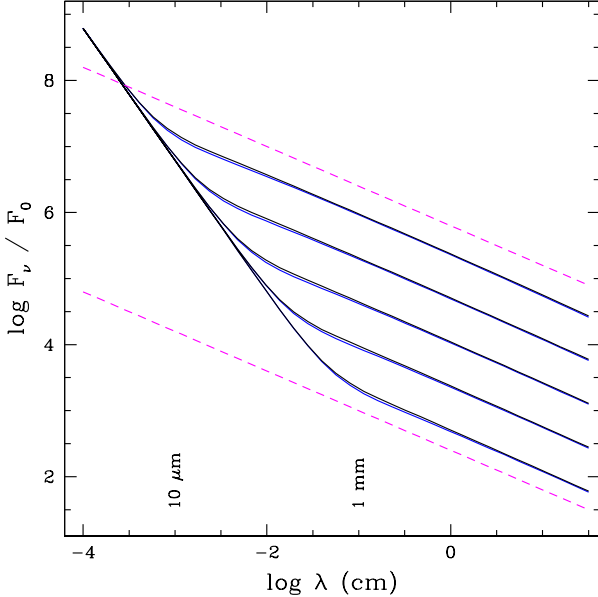


Figure 4. SED calculations that compare microclumping models with porosity models for shell fragments. All curves are for $\tau_0 = 300$, with $f_0 = 0.0001$ (top), 0.001, 0.01, 0.1, and 1.0 (bottom). The two sets of curves are so close as to be indistinguishable in this plot.

Solid lines are for the shell fragments; dashed lines are for microclumping using the same parameters. The radial width of a shell fragment is chosen to be $\delta l_0 = f_0$. The upper panel shows curves for the full range of u ; lower is a blow-up around the region of optical depth unity. Differences between micro-

clumping and porosity with shell fragments only begins to develop near optical unity; departures between the two then increase toward higher optical depth.

The right side of Figure 3 displays a cross-section of the axisymmetric optical-depth unity contours in the $z - p$ plane. The colors and line types correspond to those of the left side of the figure. The central hashed region is for a smooth, unclumped wind with the same value of τ_0 . Note that the contours are fairly closely matched, save for the “dimple” that results for the shell fragments. That feature arises where shell fragments are seen more nearly edge-on so that the porosity length is large.

Figure 4 shows model SEDs for both microclumping and for porosity with shell fragments. The optical depth parameter $\tau_0 = 300$ is the same as in Figure 3, but a greater range of volume filling factors are used to spread out the transition in wavelength from star-dominated to wind-dominated continua. For Figure 4, the filling factor constant ranges from $f_0 = 10^0$ (lowest curve) to 10^{-4} (highest curve). Note that the transition from star-dominated to wind-dominated would sample the inner, accelerating portion of the wind, which is not currently included in the model. Such effects are ignored to emphasize comparisons between microclumping and macroclumping effects.

The two sets of SEDs are so close as to be indistinguishable in the figure. That microclumping and porosity with shell fragments yield essentially identical SEDs aligns well with the fact that the two models have such close los optical depths for the optically thin portion of the wind.

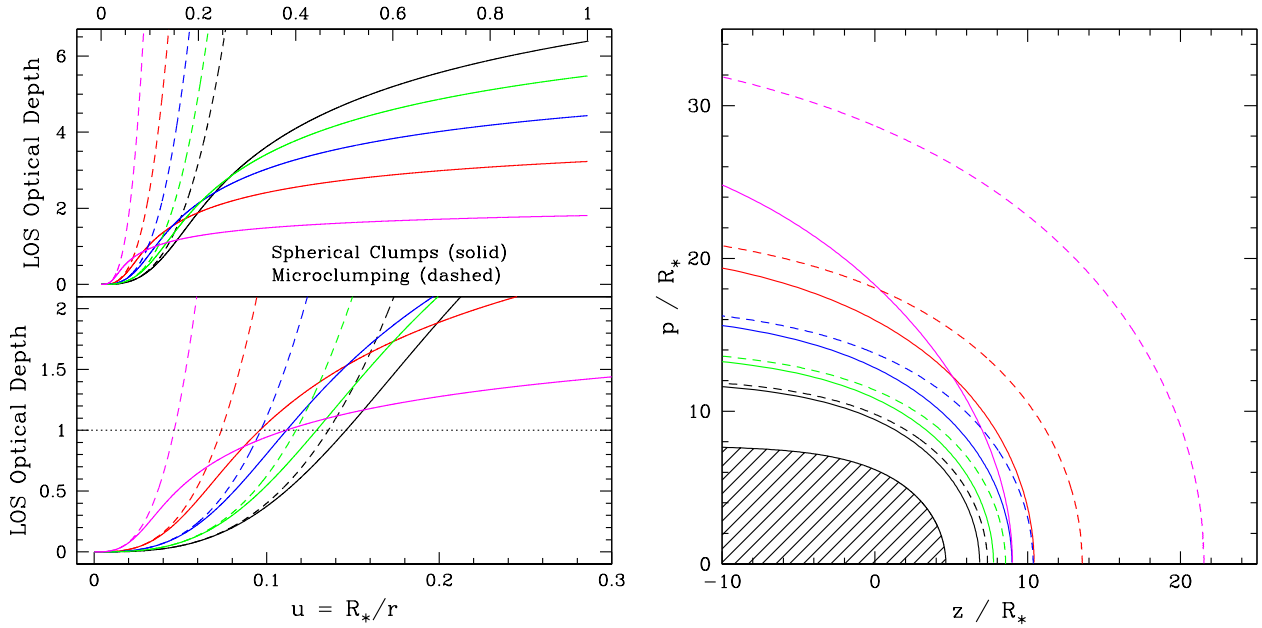


Figure 5. The models here are like those in Fig. 3, but for porosity with spherical clumps. The models have the same value of $\tau_0 = 300$, f_V has the same range of values as did f_0 , with the same corresponding color designations. Major differences as compared to shell fragments are (a) the overall lower optical depths achieved at the star, (b) the fact that departures between microclumping and the porosity start at lower optical depths of only a few tenths, and (c) the crossing of curves, both in the los optical depths (left) and in some cases the contour curves (right).

4.2 Porosity with Spherical Clumps

The nature of spherical clumps is different from the case of shell fragments. For spheres the volume filling factor is given by

$$f_V = n_{cl}(r) V_{cl} = \frac{1}{3} \frac{\dot{N}_0}{v_\infty / R_*} \tilde{R}_0^3, \quad (47)$$

where $n_{cl} \propto r^{-2}$, $V_{cl} \propto r^2$, \tilde{R}_0 is the normalized radius of a clump as the base of the wind. Whereas shell fragments have a volume filling factor that does not depend on radius from the star, but does depend on location about the star, owing to their flattened shapes, the f_V for spheres is the same at all locations. The related porosity length scales as:

$$\tilde{h} = \frac{1}{n_{cl} A_{cl} R_*} = 4 \left(\frac{v_\infty / R_*}{\dot{N}} \right) \left(\frac{1}{\tilde{R}_0^2} \right) \tilde{r}^{2/3} = \frac{4}{3} \frac{\tilde{R}_0}{f_0} u^{-2/3}. \quad (48)$$

which has the inverse scaling with radius as the clump solid angle. Consequently, the porosity length becomes larger with increasing distance from the star.

For spheres the lines of sight intersect the spherical clumps along different chords. Noting that τ_{cl} is the optical depth along the diameter of a spherical clump, Appendix B details the analytic derivation for the inner integral for equation (40). The result, simply stated here, is that

$$\tau = \int n_{cl} A_{cl} R_* G(\tau_c) dz, \quad (49)$$

where

$$G(\tau_{cl}) = 1 - \frac{2}{\tau_{cl}} [1 - e^{-\tau_{cl}} - \tau_{cl} e^{-\tau_{cl}}]. \quad (50)$$

The optical depth integral can be more conveniently expressed as

$$\tau = \frac{\tau_0}{f_V} \frac{1}{\tilde{p}^3} \int_0^\theta \left[\frac{3G(\tau_{cl})}{2\tau_{cl}} \right] \sin^2 \theta d\theta, \quad (51)$$

where as before, $\tan \theta = \tilde{p}/\tilde{z}$. The ratio $3G/2\tau_c$ acts like an escape probability for the clump. When $\tau_{cl} \ll 1$, the ratio $3G/2\tau_{cl}$ reduces to unity, as expected for optically thin clumps. When $\tau_{cl} \gg 1$, the ratio becomes $1/(2\tau_c/3)$. The factor of $2/3$ arises from area-averaging the optical depth across the face of the spherical clump.

Along the los to the star, the optical depth expression becomes

$$\tau(u) = \frac{\tau_0}{f_V} \int_0^u \left[\frac{3G(\tau_{cl})}{2\tau_{cl}} \right] u^2 du, \quad (52)$$

The optical depth across the diameter of the clump is

$$\tau_{cl} = \left(\frac{\tau_0}{f_V} \right) \left(\frac{2\tilde{R}_{cl}}{f_V} \right) u^{10/3}. \quad (53)$$

The unusual power-law exponent with radius derives from how the spherical clump evolves in size throughout the wind, as explained next.

To illustrate the effects of porosity with spherical clumps, Figure 5 shows the los optical depth in the porosity

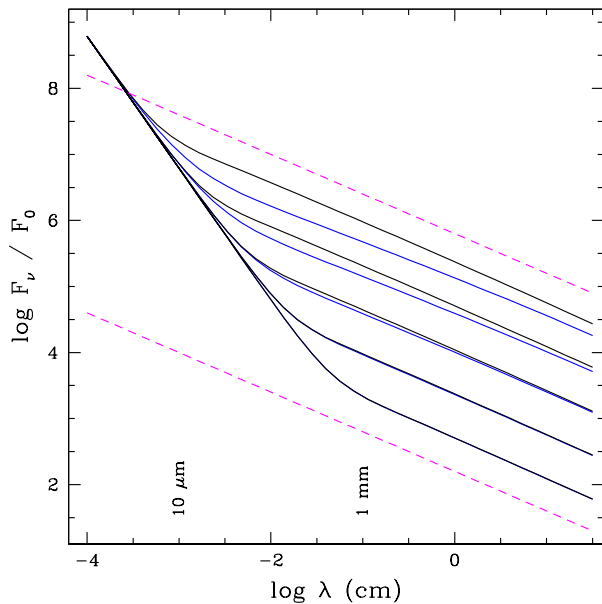


Figure 6. Model SEDs to compare microclumping (black) and porosity with spherical clumps (blue). The models are for τ_0 and f_V values used in Fig. 5. The SEDs with spherical clumps achieve the same asymptotic slopes as for microclumping, but at lower flux levels. The discrepancy in the flux level worsens as f_V becomes smaller.

formalism. The figure is similar to Figure 3 for shell fragments, with the same τ_0 , the same range in f_V , and the same color scheme. Again, the dotted curves are for microclumping. The clump radii scale as $\bar{R}_0 = 0.03 (f_V/0.01)^{1/3}$. For low optical depths, the curves closely follow each other as expected. Departures between microclumping and porosity develop around \log optical depth of a couple tenths. When f_V is small, optical depth unity for the spherical clumps occurs at a notably smaller radius than for microclumping; for shell fragments optical depth unity occurred close in radius to the microclumping result.

The right side of Figure 5 displays corresponding optical depth unity contours for the $z-p$ plane. The colors are the same as for the left figure. Rearward of the star (large negative values of z), the contours are sequenced in terms of f_V , with the highest filling factor (least porous wind) being more compact, and smallest filling factor (most porous wind) being larger. The optical depth unity contours for microclumping with the same value of τ_0 and f_V can lie at larger radii when f_V is small. Consequently, porosity with spherical clumps indicates that the bulk of the long-wavelength emission arises from a more compact region of the wind as compared with microclumping.

Figure 6 shows SED calculations that contrast microclumping with a porous wind consisting of spherical clumps. The microclumping results are the black lines, and the porous wind results are shown in blue. Unlike the case for shell fragments, there can be noticeable differences in flux levels. There are several key points to be made about these results.

- There is no distinction between microclumping and porosity when $f_V = 1$ (lowest curve).

- When departures between microclumping and porosity do arise, the differences are greater for smaller values of f_V .
- The differences are greatest at wavelengths around the transition from star-dominated to wind-dominated SEDs.
- The SEDs with porosity tend toward the SEDs with microclumping at sufficiently long wavelengths.
- At wavelengths where departures are significant, the SED slope is *more shallow* than the canonical slope of -0.6 value for the power-law SED.

- Figure 7 contrasts the cases of shell fragments and spherical clumps. Plotted is the relative differential flux contribution dF_V/dp with impact parameter p as normalized by R_* , with

$$\frac{dF_V}{dp} \propto p \left[1 - e^{-\tau(p)} \right].$$

The upper panel compares shell fragments (dashed) with microclumping (solid); lower compares spherical clumps (dashed) with microclumping (again solid). The curve for shell fragments closely matches the one for microclumping; with spherical clumps there is a greater difference. The latter arises because the run of total effective optical depth achieved with spherical clumps is lower than for shell fragments.

In Figure 6, with $f_V = 0.0001$, the slope for the porous model SED, between $\log \lambda$ of -1 and $+1$, is very close to -0.55 , which is the value expected in the sparse limit for an inverse square density (i.e., $m = 2$) from § 3.2. That departures between the microclumping and porosity SEDs increase with decreasing f_V is a reflection of the idea that the sparse limit is becoming a better approximation for the clump distribution. At sufficiently long wavelengths, there are more optically thick clumps, and the sparse limit no longer remains valid.

For a given value of \dot{M} , a porous wind with spherical clumps can yield a lower flux level as compared to microclumping. Ignoring porosity effects and adopting the assumption of microclumping would then require a lower value of \dot{M} (or, a larger value of f_V) to match the observed SED flux level. However, the effect is only significant at fairly extreme values of f_V . With $f_V = 0.001$, the SED with porosity differs from the microclumping one by less than 0.2 dex. Also, the severity of the departure between the cases depends on λ .

5 CONCLUSION

All else being equal (isothermal, constant velocity, no ionization gradients), the geometry of clumps can influence IR/radio fluxes and power-law SED slopes when porosity effects are included. One should generally expect macroclumping effects to become important at sufficiently long wavelengths, since the free-free opacity grows as λ^2 .

If the clumps take the form of shell fragments, both the SED flux levels and SED slope are essentially identical to the microclumping case. For the shell fragment geometry, the \log optical depth with porosity close tracks with that of the microclumping case below optical unity. The optical unity contours closely follow those for microclumping. In the

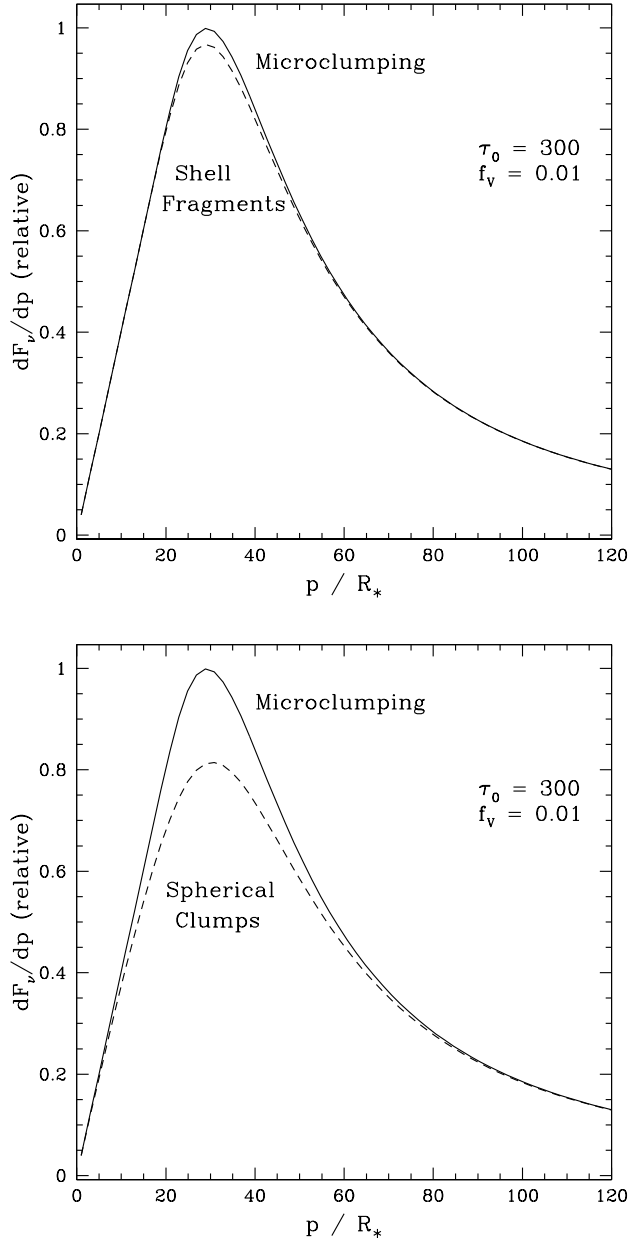


Figure 7. A comparison of SEDs with porosity for shell fragments (upper) versus spherical clumps (lower) in terms of dF_ν/dp (see text) versus impact parameter p/R_* . For both panels the solid curve is for microclumping, and the dashed curves include porosity effects. The models are for $\tau_0 = 300$ and $f_V = 0.01$. The curve for shell fragments much more closely follows the curve for microclumping; the curve for spherical clumps shows a greater deviation. The smaller fluxes with porosity arise from the smaller effective optical depths as compared to microclumping. At large p , the curves closely match where clumps become optically thin; at small p , the curves closely match because even with porosity, the effective optical depth becomes large.

“pseudo-photosphere” picture, the optical depth unity surface for microclumping and for porosity with shell fragments are very similar in spatial extent, and the resultant fluxes end up nearly the same over a wide range of volume filling factors.

By contrast, spherical clumps can yield results that are distinct from the case of microclumping. Unlike the case of shell fragments that have a constant porosity length in the asymptotic wind, \tilde{h} is not constant for spherical clumps for an inverse square law density. The case of porosity with spherical clumps still achieves the canonical slope of -0.6 , but departures between SEDs with porosity and those that assume microclumping can arise at some wavelengths. The range of wavelengths over which the differences occur, and the amplitude of the difference depends strongly on the value of f_V . Achieving a flux difference in excess of 0.1 dex requires $f_V < 0.01$; significant differences only result for rather extreme volume filling factors, of order 10^{-4} . And, when those differences arise, it is because the so-called “sparse limit” is being achieved. The result is a power-law SED slope that, for an inverse square law density, is more shallow than the canonical value of -0.6 .

ACKNOWLEDGEMENTS

Ignace is grateful to an anonymous referee for several helpful comments, and to Maurice Leutenegger for having made a number of insightful points on an earlier manuscript. Ignace recognizes support for this research through a grant from the National Science Foundation (AST-0807664).

APPENDIX A: ANALYTIC SED SOLUTIONS FOR SMOOTH WIND CASES

In the limiting case of large optical depth, [Wright & Barlow \(1975\)](#) and [Panagia & Felli \(1975\)](#) showed that the integration for the flux of wind emission becomes analytic when $\kappa_\nu \rho \propto r^{-4}$, for r the radius in the wind. In this case the optical depth along a los becomes $\tau_\nu = a_0 \tau_0(\lambda) \tilde{p}^{-3}$, where a_0 is a constant, τ_0 is the optical scaling at wavelength λ , and \tilde{p} is the normalized impact parameter for the sightline. The approach can be generalized for \tilde{p} raised to other powers.

The integral to be evaluated is:

$$F_\nu = 2\pi \frac{R_*^2}{D^2} B_\nu(T_w) \int_0^\infty \left(1 - e^{-k_\lambda \tilde{p}^\alpha}\right) \tilde{p} d\tilde{p}, \quad (\text{A1})$$

where $k_\lambda \propto \tau_0(\lambda)$ and α is the power-law exponent.

This integral has an analytic solution of

$$F_\nu = 2\pi \frac{R_*^2}{D^2} B_\nu(T_w) \left[-\frac{1}{\alpha} \Gamma\left(\frac{-2}{\alpha}\right) k^{-2/\alpha} \right] \quad (\text{A2})$$

If $\alpha > 2$, the recursion relation $\Gamma(1+x) = x\Gamma(x)$ can be used to show that the bracketed term is indeed positive, with

$$-\frac{1}{\alpha} \Gamma\left(\frac{-2}{\alpha}\right) = \frac{2}{\alpha^2} \Gamma\left(\frac{\alpha-2}{\alpha}\right). \quad (\text{A3})$$

APPENDIX B: THE SPHERICAL MACROCLUMP

Discussions of macroclumping in stellar winds often adopt isotropic or fragment clumps. An analytic solution can be derived for a spherical clump of uniform density that takes account of variations in optical depth with chord length for use in the porosity formalism. The optical depth along a chord through a spherical clump is

$$t_{\text{cl}} = \frac{\tau_0}{f_V^2} \times 2 \delta \tilde{z} \times \tilde{r}^{-4}, \quad (\text{B1})$$

where all lengths are scaled to the stellar radius R_* , and $2\delta\tilde{z}(\tilde{\omega})$ is the pathlength for a chord at impact parameter, $\tilde{\omega}$. Using eq. (40), the optical depth through a wind consisting of spherical clumps is

$$\tau = \int n_{\text{cl}}(r) R_*^3 \left\{ \int_0^{\tilde{R}_{\text{cl}}} [1 - e^{-t_{\text{cl}}(\delta\tilde{z})}] 2\pi \tilde{\omega} d\tilde{\omega} \right\} d\tilde{z}, \quad (\text{B2})$$

for n_{cl} the number density of clumps. The inner integral relates to the area-weighted probability of a photon being absorbed by the clump with optical depth t_{cl} . Noting that $\delta z = \sqrt{\delta x_c^2 - \tilde{\omega}^2}$, the preceding integral can be written as

$$\tau = \int n_{\text{cl}}(\tilde{r}) R_*^3 \left[\pi \tilde{R}_{\text{cl}}^2 - 2\pi \int_0^{\tilde{R}_{\text{cl}}} e^{-q(\tilde{r}) \delta\tilde{z}} \delta\tilde{z} d\delta\tilde{z} \right] d\tilde{z}, \quad (\text{B3})$$

where a change of variable has been used to eliminate $\tilde{\omega}$ in favor of $\delta\tilde{z}$. The second term in brackets is of the form

$$\tau = \int x e^{-qx} dx. \quad (\text{B4})$$

This expression has an analytic solution, after which the los optical depth reduces to

$$\tau = \int_{\tilde{z}_0}^{\infty} n_{\text{cl}}(x) R_*^3 \left\{ 1 - \frac{2}{\tau_{\text{cl}}} [1 - (1 + \tau_{\text{cl}}) e^{-\tau_{\text{cl}}}] \right\} d\tilde{z}, \quad (\text{B5})$$

with τ_{cl} the optical depth across the diameter of a clump located at radius r . The term in braces is $G(\tau_{\text{cl}})$ from eq. (29). The final result for the los optical depth is

$$\tau = \int_{\tilde{z}_0}^{\infty} \left[\frac{2G(\tau_{\text{cl}})}{3\tau_{\text{cl}}} \right] u^4 d\tilde{z}, \quad (\text{B6})$$

where $u = \tilde{r}^{-1}$. A change of variable from \tilde{z} to polar angle θ yields eq. (51).

REFERENCES

Abbott D. C., Biegging J. H., Churchwell E., 1981, *ApJ*, **250**, 645
 Abbott D. C., Biegging J. H., Churchwell E., Torres A. V., 1986, *ApJ*, **303**, 239
 Biegging J. H., Abbott D. C., Churchwell E. B., 1989, *ApJ*, **340**, 518
 Blomme R., 2011, *Bulletin de la Societe Royale des Sciences de Liege*, **80**, 67
 Blomme R., Runacres M. C., 1997, *A&A*, **323**, 886

Bonanos A. Z., et al., 2009, *AJ*, **138**, 1003
 Bouret J.-C., Lanz T., Hillier D. J., 2005, *A&A*, **438**, 301
 Brown J. C., Richardson L. L., Antokhin I., Robert C., Moffat A. F. J., St-Louis N., 1995, *A&A*, **295**, 725
 Brown J. C., Barrett R. K., Oskinova L. M., Owocki S. P., Hamann W.-R., de Jong J. A., Kaper L., Henrichs H. F., 2004a, *A&A*, **413**, 959
 Brown J. C., Cassinelli J. P., Li Q., Kholtygin A. F., Ignace R., 2004b, *A&A*, **426**, 323
 Cassinelli J. P., Hartmann L., 1977, *ApJ*, **212**, 488
 Cassinelli J. P., Swank J. H., 1983, *ApJ*, **271**, 681
 Castor J. I., Abbott D. C., Klein R. I., 1975, *ApJ*, **195**, 157
 Cox A. N., 2000, *Allen's astrophysical quantities*
 Davies B., Vink J. S., Oudmaijer R. D., 2007, *A&A*, **469**, 1045
 Dessart L., Owocki S. P., 2003, *A&A*, **406**, L1
 Dessart L., Owocki S. P., 2005, *A&A*, **437**, 657
 Drew J. E., 1989, *ApJS*, **71**, 267
 Ellinger C. I., Young P. A., Fryer C. L., Rockefeller G., 2012, *ApJ*, **755**, 160
 Feldmeier A., Puls J., Pauldrach A. W. A., 1997, *A&A*, **322**, 878
 Feldmeier A., Oskinova L., Hamann W.-R., 2003, *A&A*, **403**, 217
 Fullerton A. W., Massa D. L., Prinja R. K., 2006, *ApJ*, **637**, 1025
 Gayley K. G., 2012, in Drissen L., Robert C., St-Louis N., Moffat A. F. J., eds, *Astronomical Society of the Pacific Conference Series Vol. 465, Proceedings of a Scientific Meeting in Honor of Anthony F. J. Moffat*. p. 140
 González R. F., Cantó J., 2008, *A&A*, **477**, 373
 Hamann W.-R., Koesterke L., 1998, *A&A*, **335**, 1003
 Hamann W.-R., Feldmeier A., Oskinova L. M., eds, 2008, *Clumping in hot-star winds*
 Hillier D. J., 1991, *A&A*, **247**, 455
 Hillier D. J., Jones T. J., Hyland A. R., 1983, *ApJ*, **271**, 221
 Hirschi R., 2008, in Hamann W.-R., Feldmeier A., Oskinova L. M., eds, *Clumping in Hot-Star Winds*. p. 9 ([arXiv:0709.0392](https://arxiv.org/abs/0709.0392))
 Ignace R., 2001, *ApJ*, **549**, L119
 Ignace R., 2009, *Astronomische Nachrichten*, **330**, 717
 Ignace R., Churchwell E., 2004, *ApJ*, **610**, 351
 Ignace R., Gayley K. G., 2002, *ApJ*, **568**, 954
 Ignace R., Quigley M. F., Cassinelli J. P., 2003, *ApJ*, **596**, 538
 Ignace R., Waldron W. L., Cassinelli J. P., Burke A. E., 2012, *ApJ*, **750**, 40
 Krtićka J., Kubát J., 2012, *MNRAS*, **427**, 84
 Leitherer C., Chapman J. M., Koribalski B., 1995, *ApJ*, **450**, 289
 Lépine S., Moffat A. F. J., 1999, *ApJ*, **514**, 909
 Leutenegger M. A., Owocki S. P., Kahn S. M., Paerels F. B. S., 2007, *ApJ*, **659**, 642
 Leutenegger M. A., Cohen D. H., Sundqvist J. O., Owocki S. P., 2013, *ApJ*, **770**, 80
 Li Q.-K., Cassinelli J. P., Brown J. C., Ignace R., 2009, *Research in Astronomy and Astrophysics*, **9**, 558
 Lucy L. B., Solomon P. M., 1970, *ApJ*, **159**, 879
 Lucy L. B., White R. L., 1980, *ApJ*, **241**, 300
 Lupie O. L., Nordsieck K. H., 1987, *AJ*, **93**, 214
 Macfarlane J. J., Cassinelli J. P., 1989, *ApJ*, **347**, 1090
 Massa D., et al., 1995, *ApJ*, **452**, L53
 Mohamed S., Mackey J., Langer N., 2012, *A&A*, **541**, A1
 Muijres L. E., Vink J. S., de Koter A., Müller P. E., Langer N., 2012, *A&A*, **537**, A37
 Nazé Y., Oskinova L. M., Gosset E., 2013, *ApJ*, **763**, 143
 Nugis T., Crowther P. A., Willis A. J., 1998, *A&A*, **333**, 956
 Oskinova L. M., Feldmeier A., Hamann W.-R., 2004, *A&A*, **422**, 675
 Oskinova L. M., Hamann W.-R., Feldmeier A., 2007, *A&A*, **476**, 1331
 Osterbrock D. E., 1989, *Astrophysics of gaseous nebulae and active galactic nuclei*
 Owocki S. P., Cohen D. H., 2001, *ApJ*, **559**, 1108
 Owocki S. P., Cohen D. H., 2006, *ApJ*, **648**, 565

- Owocki S. P., Castor J. I., Rybicki G. B., 1988, *ApJ*, **335**, 914
Owocki S. P., Gayley K. G., Shaviv N. J., 2004, *ApJ*, **616**, 525
Panagia N., Felli M., 1975, *A&A*, **39**, 1
Pauldrach A., Puls J., Kudritzki R. P., 1986, *A&A*, **164**, 86
Prinja R. K., Howarth I. D., 1986, *ApJS*, **61**, 357
Prinja R. K., Barlow M. J., Howarth I. D., 1991, *ApJ*, **383**, 466
Prinja R. K., Massa D. L., Urbaneja M. A., Kudritzki R.-P., 2012, *MNRAS*, **422**, 3142
Puls J., Markova N., Scuderi S., Stanghellini C., Taranova O. G., Burnley A. W., Howarth I. D., 2006, *A&A*, **454**, 625
Runacres M. C., Owocki S. P., 2002, *A&A*, **381**, 1015
Sundqvist J. O., Puls J., Feldmeier A., 2010, *A&A*, **510**, A11
Sundqvist J. O., Owocki S. P., Cohen D. H., Leutenegger M. A., Townsend R. H. D., 2012, *MNRAS*, **420**, 1553
Sundqvist J. O., Puls J., Owocki S. P., 2014, *A&A*, **568**, A59
Taylor M., Nordsieck K. H., Schulte-Ladbeck R. E., Bjorkman K. S., 1991, *AJ*, **102**, 1197
Waldron W. L., Cassinelli J. P., 2010, *ApJ*, **711**, L30
Wright A. E., Barlow M. J., 1975, *MNRAS*, **170**, 41
Zsargó J., Hillier D. J., Bouret J.-C., Lanz T., Leutenegger M. A., Cohen D. H., 2008, *ApJ*, **685**, L149
Šurlan B., Hamann W.-R., Aret A., Kubát J., Oskinova L. M., Torres A. F., 2013, *A&A*, **559**, A130